Applied Surface Science 528 (2020) 147059

Contents lists available at ScienceDirect

Applied Surface Science

journal homepage: www.elsevier.com/locate/apsusc

Activation characterization of the Ti-Zr-V getter films deposited by magnetron sputtering

Sihui Wang[a], Zhiwei Wang[b], Xin Shu[c], Wei Wei[a,*], Yonghao Gao[d], Yong Wang[a]

[a] National Synchrotron Radiation Laboratory, University of Science and Technology of China, HeFei 230029, PR China
[b] School of Mechanical Engineering, Hefei University of Technology, Hefei 230031, PR China
[c] Hunan Aerospace TianLu Advanced Materials Testing Co,. Ltd., Changsha 410000, PR China
[d] School of Materials Science and Engineering, Central South University, Changsha 410083, PR China

ARTICLE INFO

Keywords:
Ti-Zr-V
Non-evaporable getter films
XPS
Activation

ABSTRACT

Non-evaporable getter (NEG) thin films provide distributed pumping properties, allowing to achieve ultrahigh vacuum in narrow and conductance limited chambers. It is an ideal solution to deal with the small aperture of vacuum chambers. In this paper, ternary Ti-Zr-V getter film with approximate equal atomic ratio was deposited on oxygen free copper (OFC) substrate by using a developed DC magnetron sputtering system with an alloy target. Microstructural characterization by scanning electron microscopy, atomic force microscopy and energy dispersive spectroscopy (EDX) indicates that the porous getter film exhibit a columnar growth pattern and the grain sizes are very distributed ranging from several up to hundreds of nanometres. The compositions and the corresponding chemical bonding states are analyzed by using *in-situ* synchrotron radiation X-ray photoelectron spectroscopy after activation for 1 h at different temperatures in ultra-high vacuum. The results indicate that Ti, Zr and V are initially in their high oxidized states, which are gradually reduced in steps to oxides of lower valence states and finally to their metallic states. The reduction of vanadium oxides is more preferable than that of titanium- and zirconium-oxides. Such activation commences at a temperature as low as 150 °C, and can be enhanced by increasing temperature.

1. Introduction

Deposition of non-evaporable getter (NEG) films effectively transfers the inner wall of vacuum chamber and cavities into distributed pumps, thus providing a well-recognized solution to the problems associated with residual gas (O_2, H_2, CO, N_2, etc.) control [1–6]. Therefore, it is possible to achieve ultra-high vacuum desirable for the advanced accelerators and vacuum packaged MEMs devices.

However, the surface of the NEG thin films are readily to be oxidized and contaminated upon exposure to ambient conditions due to its high oxygen affinity. As a consequence, its ability of further chemisorption is rather limited as the oxide layer not only consumes the active sties to interact with the surrounding residual gases, but also acts as a barrier hindering the diffusion of gases into the bulk materials [7], which, unfortunately, has been acknowledged as the two essential processes leading to its high absorption capacity. The generally accepted practice to restore the sorption capacity of the NEG films is by thermal activation realized by simple baking [8–10], during which, the oxides gradually diffuse towards the bulk, leaving free surface sites to interact with the residual gases.

However, it is of importance that the annealing temperature should be compatible with the accelerator operation [11,12]. Specifically, the vacuum chambers of the accelerators are normally made of metallic alloys, like stainless steel, aluminum alloys, oxygen-free copper (OFC), etc. The mechanical properties of these metallic parts drop drastically with temperature. For example, when the temperature increased from room temperature to 200 °C, the yield strength of OFC is almost halved [13], therefore, it is critical to lower the activation temperature in order to maintain the mechanical integrity of the vacuum chamber. On the other hand, too high temperature is also detrimental causing reduced lifetime of the instruments attached to the chamber.

Tremendous efforts have been devoted towards lowering the activation temperature of the NEG films [11,12], either by manipulating their chemical composition [14] or by tailoring their microstructural characteristics through adjusting the corresponding deposition parameters [15]. Transition metals and their alloys are the most promising getter materials for residual gas removal in vacuum chambers and the widely accepted getter materials are normally composed of Ti, Zr and V.

* Corresponding author.
E-mail address: platowei@ustc.edu.cn (W. Wei).

https://doi.org/10.1016/j.apsusc.2020.147059
Received 25 March 2020; Received in revised form 19 June 2020; Accepted 22 June 2020
Available online 25 June 2020
0169-4332/

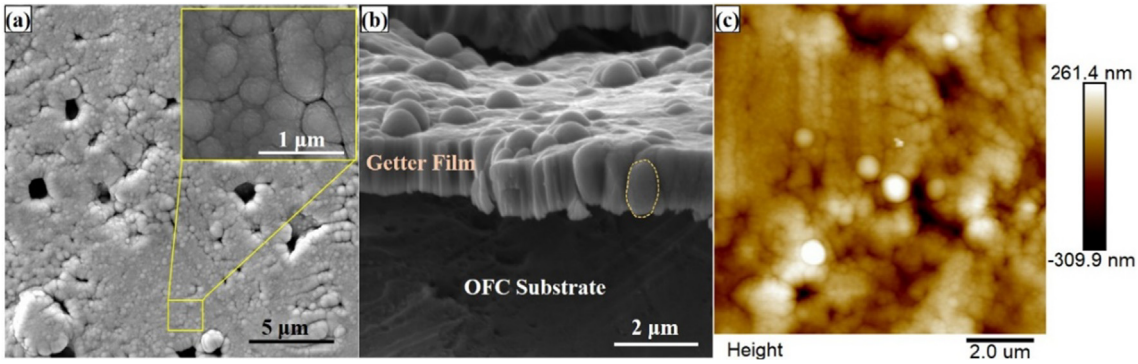

Fig. 1. (a) Surface, (b) cross sectional and (c) AFM images of the Ti-Zr-V thin films.

Ti and Zr possess high oxygen solubility thus assuring the maximum gas that can be absorbed, while V is selected because it provides high oxygen diffusivity that guarantees acceptable activation kinetics. Deposition parameters leading to refined grains, amorphous structures [10] and/or high porosity [16] are preferred as the oxygen diffusion might be enhanced along the grain boundaries and pores [9,10]. It has been published that ternary Ti-Zr-V thin film normally has an activation temperature within the range of 180 ~ 400 °C [17–19], depending on the specific composition and thin film microstructures.

Then, the persisting question remains as if it is possible to further reduce the activation temperature. In the present work, the activation process of Ti-Zr-V thin films deposited on OFC substrates starts at a temperature as low as 150 °C after quantitative analysis of the chemical states evolution on the surface of the film upon annealing by in-situ synchrotron radiation X-ray photoelectron spectroscopy.

2. Experimental procedures

Magnetron sputtering PVD is used to produce Ti-Zr-V thin films on OFC substrates. The coupon of a ternary Ti-Zr-V alloy wire (Φ3 mm) with a chemical composition of equal atomic ratio is used as the target. Before deposition the OFC substrates are carefully cleaned by dipping in alkaline solution and subsequent acid etching in an ultrasonic bath so as to increase the adhesion strength of the thin films. No pre-heating is conducted on the substrate to promote the formation of refined grains and increased surface roughness [20]. The background base pressure in the deposition chamber before sputtering is 5×10^{-5} Pa. The thin films are deposited using pulsed unipolar current mode. The applied current are kept constant at 0.1 A, the duty cycle are pre-set to be 38.5%, and the corresponding frequency is 50 Hz. The magnetic field strength used for the deposition is 170 G. Kr is supplied as the sputtering gas due to its high sputtering yield [21], and the working pressure utilized in the present study is 1 Pa.

The surface and cross-sectional morphologies of the thin films are characterized by using Tescan MAIA3 schottky field emission scanning electron microscopy equipped with Oxford Instruments X-Max 50 energy dispersive spectroscopy (EDS) for chemical analysis. As the OFC substrate is very ductile while the getter film is brittle, the samples are bended so as to expose getter flakes, from which the cross-sectional images of the thin film are acquired. The film thickness are measured directly from the cross-sectional SEM images. The roughness of the films are evaluated using DI Innova scanning probe microscope operated in non-contact tapping mode and phase mode under ambient conditions.

In-situ synchrotron radiation X-ray photoelectron spectroscopy characterization is performed with a VG-ScientaR3000 hemispherical analyzer using non-monochromatic Mg K radiation (1253.6 eV) as excitation source to identify the evolution of chemical states within the top surface of the thin films while being annealed at different temperatures from 150 °C to 180 °C at an interval of 10 °C. XPS data was collected step by step from the same sample after annealing for 1 h at pre-set temperatures with a chamber pressure of 1.5×10^{-7} mbar. High-resolution spectra for the Ti 2*p*, Zr 3*d*, and C 1*s* orbitals was individually collected within their respective binding energy ranges, while that for the V 2*p* and O 1*s* regions are collected together in the binding energy ranging from 509 to 538 eV.

The resulting XPS data are analyzed and fitted using CasaXPS software. A C 1*s* core level orbital is used as the charging reference at a binding energy of 284.5 eV. Shirley background is subtracted for all the collected spectra. V 2*p* + O 1*s* spectra is fitted together using a single Shirley background subtraction to improve the fitting reliability. The measured XPS spectra is resolved to reveal the chemical states. Gaussian (Y%)–Lorentzian (X%) profiles are used to model the symmetric peak shapes, while the function LA(α,β,m) defined in CasaXPS is selected for the asymmetric peaks yielded from metallic cores (M^0). Following the literature [22], LA(1.1,5,7) and LA(1.2,5,8) profiles are selected to model the spectrum of Ti^0 and V^0, respectively. For the Ti 2*p* and V 2*p* orbitals, the intensities of the 2*p*3/2 with respect to 2*p*1/2 peaks is strictly constrained following the ~2:1 ratio relation, while the peak intensities for the Zr 3*d*5/2 splitting is set to be 1.5 times that of the Zr 3*d*3/2 splitting. As the 2*p*3/2 and 3*d*5/2 peaks are, respectively, much more intense than that of 2*p*1/2 and 3*d*3/2 peaks, only the binding energy and corresponding full width at half maximum (FWHM) of the related 2*p*3/2 and 3*d*5/2 peaks are reported in the present study. The characteristic binding energy used to resolve the measured XPS spectra is compile from the NIST Database and X-ray photoelectron spectroscopy handbook [23].

3. Results and discussion

3.1. Microstructural characterization

The surface morphology of the Ti-Zr-V thin film deposited in the present study as shown in Fig. 1(a) exhibits very porous characteristics. The surface of the thin film are composed of cauliflower-like clusters, as shown by the inset in Fig. 1(a). The pores exhibit various size without any specific geometric shapes. The analysis of the surface SEM images of much lower magnification (not shown here) using ImageJ software reveals a total porosity of about 5%, and the largest pore observed is around 15 μm^2, while the smallest ones are less than 1 μm^2. Elemental mapping analysis by EDX shows that the films is composed of 29.5 at.% Ti, 29.8 at.% V, 33.2 at.% Zr and 7.5 at.% O (O atoms are readily to be absorbed by the getter film as long as it is exposed to ambient air). All the three metallic elements are homogenously distributed within the getter film without any obvious segregation. The cross-sectional images of the thin film (Fig. 1(b)) presents columnar grain structures, as can be explained following Thornton's growth mode [24]. The thin film thickness of approx. 1 μm is measured from the cross-sectional SEM image. Also from Fig. 1(b), it is clear that the pores observed from the top surface (Fig. 1(a)) are not producing any through-holes along the

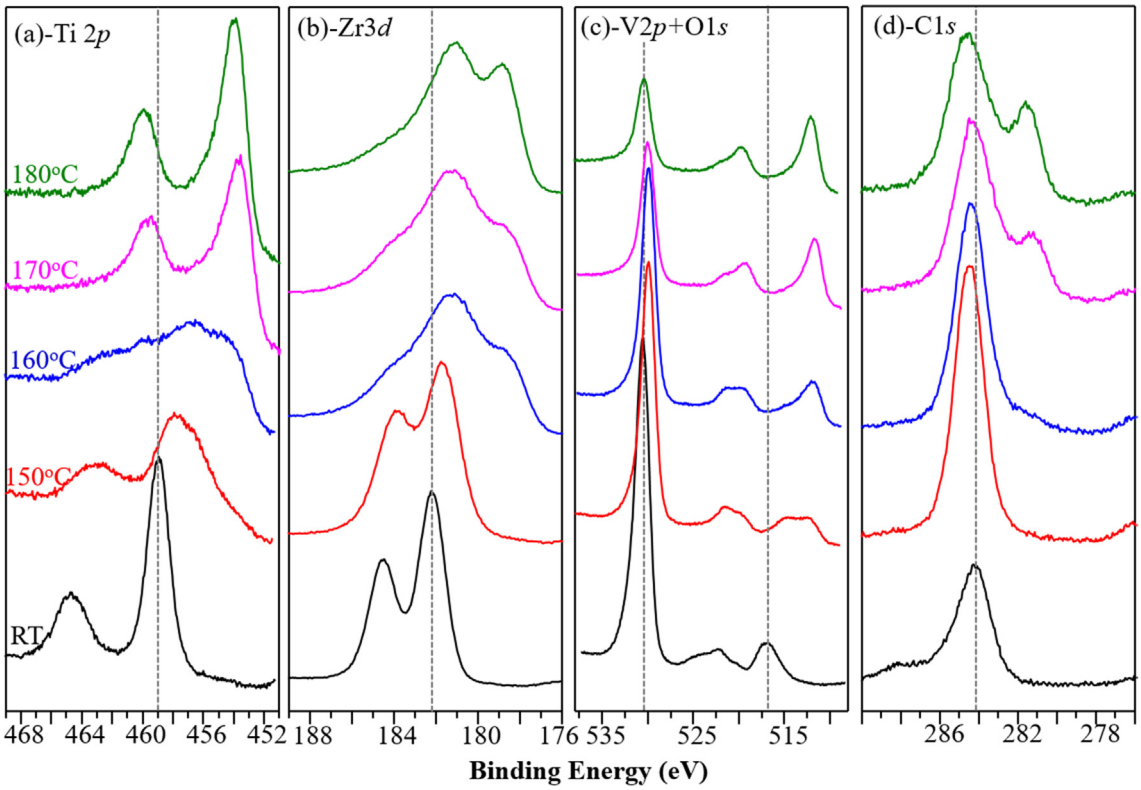

Fig. 2. Evolution of high-resolution XPS spectra collect from (a) Ti 2*p*, (b) Zr 3*d*, (c) V2*p* + O1*s* and (d) C1*s* orbitals as a function of temperature.

film thickness, as the bottom of the pore may be occupied by the deposited grains (one of which have been circled in Fig. 1(b)). Such observation also indicates that the pores are possibly formed by the competitive growth of the grains. The grain diameter estimated from the AFM image (Fig. 1(c)) lies in a range between several nanometers up to 500 nm, and a surface roughness of 59.2 nm is also yielded from Fig. 1(c). The boundaries of the columnar grains serve as direct diffusion path for the residual gases. The presence of porosity, large spreading of grain diameters together with the large surface roughness is beneficial to enhance the active surface area of the thin films. On the other hand, the large grain boundary volume arising from the nano-sized grains and the pores provides effective diffusion paths, therefore, the activation kinetics might be largely increased.

3.2. XPS investigation of as-deposited sample

XPS survey spectra reveals that the superficial surface of the thin films comprises of Ti, Zr, V, O and C, and the corresponding high-resolution XPS spectra and the evolution of valence states with increasing annealing temperature for each individual element is presented in Fig. 2. It is found that the positions of the peaks are obviously shifted and their geometric shapes evolved greatly as the annealing temperature increases. To derive the chemical states involved in the superficial surface, the collected XPS spectra is carefully resolved, as shown in Fig. 3.

In the as-deposited getter film, Ti appears in its stable oxide state TiO_2, as characterized by the 2*p*3/2 peak at binding energy of 458.9 eV (FWHM = 1.76 eV). GL(30) profile is used here to fit the symmetric peak shapes, and the separation energy for the 2*p*1/2-2*p*3/2 splitting are set to be 5.66 eV, 5.60 eV, 5.73 eV and 6.13 eV respectively for the valence state of Ti(IV), Ti(III), Ti(II) and metallic Ti (Ti^0). After resolving the spectra, it is clear that apart from the formation of TiO_2, a marginal fraction of Ti atoms are identified to be consumed by forming its sub-oxide Ti_2O_3 with the 2*p*3/2 peak at BE = 455.9 eV (FWHM = 2.0 eV). While the peak positions resolved here are in good agreement with that summarized in the literature [22,23], their FWHMs are significantly larger. Such peak broadening may be attributed either to the presence of XPS intensity distributed over many unresolved final states [25], or to the disorder within the oxide matrix [19], probably caused by a deficiency of O, as opposed to the stoichiometric oxide. By applying equal relative sensitivity factors (RSF) to the resolved 2*p*3/2 peaks and zeroing RSF for the corresponding 2*p*1/2 peaks, it is convenient to make a simple comparison of the integrated peak areas to derive that about 95% of the total Ti content in the surface exists as TiO_2, while Ti_2O_3 accounts for the rest. The dominance of TiO_2 with a small fraction of Ti_2O_3 on the top surface is the typical characteristics of the native oxide film formed with Ti alloys [26].

As for the chemical states of zirconium in the as-deposited getter film, the measured Zr3*d* profile can be deconvoluted into three doublets associated with the different oxide states. Specifically, ZrO_2 can be identified at a binding energy of 182.65 eV (FWHM = 1.38 eV) for the 3*d*5/2 peak. Apart from that, a peak with FWHM = 1.28 eV at 1 eV above that of ZrO_2 is also resolved, which can be attributed to the zirconium hydroxides ($Zr(OH)_4$), as Zr atoms are readily to interact with O and H dissolved in the metallic matrix [14] to make its surface covered with native oxide as well as a hydroxyl layer [27]. A small 3*d*5/2 peak at BE = 180.9 eV with a FWHM of 2.0 eV is also identified, which can be attributed to suboxides ZrO_x ($0 < x < 2$) [28]. The presence of ZrO_x suggests that the Zr atoms on the superficial surface is not fully oxidized in the as-deposited sample. The coexistence of zirconium oxide, suboxides and hydroxides is also supported after deconvolution of O 1*s* spectra (Fig. 3e) to reveal a main peak at binding energy of 529.06 eV (FWHM = 1.9 eV) arising from the metallic oxides (M-O), and another peak with FWHM = 2.0 eV at about +2.2 eV above the main peak associated with the OH groups [29]. Quantitative analysis reveals that the fractions of Zr atoms combined to ZrO_2, $Zr(OH)_4$ and ZrO_x are 88.2%, 9.0% and 2.8%, respectively.

From above analysis, it is now clear that Ti and Zr atoms comprising the getter films are dominantly in their full oxide state with negligible suboxides and hydroxides. The V2*p* spectrum appears apparent doublet

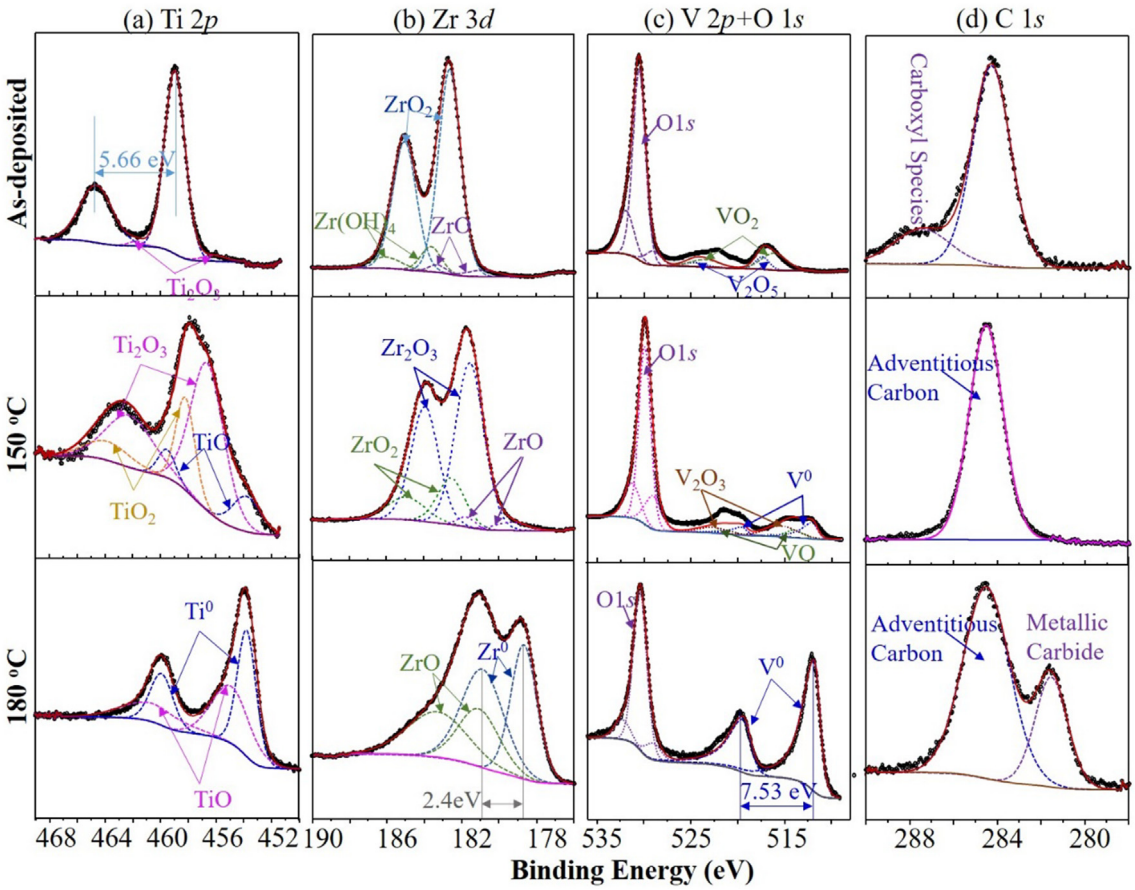

Fig. 3. Resolved XPS spectra of (a) Ti 2*p*, (b) Zr 3*d*, (c) V2*p* + O1*s* and (d) C 1*s* orbitals. The line represented by the discrete circles shows the raw data, while the red line is the synthetic envelop. The dashed lines represents the individual components resolved out of the collected spectra. (For interpretation of the references to colour in this figure legend, the reader is referred to the web version of this article.)

peaks at BE = 517.1 eV and 523.1 eV, corresponding to 2*p*3/2 and 2*p*1/2 orbitals respectively. When resolving the V2*p* + O1*s* spectrum, even though the constrains associated with the standard binding energy, theoretical energy separation and 2:1 peak area relation for the 2*p*3/2 and 2*p*1/2 doublets are carefully employed, we still obtain apparent "underfitting" of the 2*p*1/2 portion of the spectrum (Fig. 3) due to the subtraction of a single Shirley background during modelling. However the convergence of the 2*p*3/2 portion is reasonably good. In this case, it is acceptable to make the quantitative analysis only based on the 2*p*3/2 spectrum [22]. The modelling results suggests that the peak at BE = 517.1 eV can be resolved into two component peaks at binding energy of 516.1 eV (FWHM = 3.2 eV) and 517.7 eV (FWHM = 1.7 eV), originating, respectively, from the presence of VO_2 and V_2O_5 oxides (Fig. 3). Comparing the associated areas under 2*p*3/2 peaks originating from the two oxide states (RSFs of the 2*p*1/2 peaks are set to be 0) suggests that only 23.3% of V atoms are oxidized to V_2O_5, while the rest is in its suboxide state (VO_2), such observation is in agreement with Wu's [30] work that reported the dominance of suboxides of vanadium on getter film surface.

As for the spectra measured from the C 1*s* core level orbital, it is straightforward to identify a strong peak with a much weaker shoulder. After resolving the collected data, it is easy to determine that the main peak at BE = 284.2 eV (FWHM = 2.0 eV) arise from adventitious carbon contamination on the film surface, and the much broader shoulder peak (FWHM = 3.4 eV) at a binding energy of 287.3 eV is attributed to the carboxyl species attached to the getter surface [7].

3.3. Activation evaluation by XPS

It is obvious that the surface chemical states evolves drastically as the getter films are baked even by simple vision inspection of the resulting XPS spectra (Fig. 2). As for Ti 2*p* spectra, when the temperature increases to 150 °C, the position of the Ti 2*p* orbital has shifted towards lower binding energy and the FWHMs of the Ti 2*p*3/2 peaks have more than doubled as compared with that in the as-deposited film. Similar changes are also very pronounced even by a slight increase in annealing temperature by just 10 °C to 160 °C, the position of the peaks are shifted even further towards the lowering binding energy, and the associated FWHMs are so large that it is hard to distinguish the 2*p*3/2 and 2*p*1/2 peaks by simple vision inspection. After further increasing the annealing temperature to170 °C, the peaks are located at further lower binding energy and become sharp and distinguishable again, with the FWHM only slightly larger than that in its initial as-deposited condition. Further increasing the temperature to 180 °C, the peak profile of the measured spectra do not present too much changes, apart from that the peaks has shifted back a little bit by 0.5 eV and become even sharper. As previously reported [7], the shifting of peaks towards lower binding energy indicates the reduction of the Ti oxides. The spreading of FWHMs results from the co-existence of TiO_2 and its various sub-oxides TiO_x ($0 < x < 2$) [25,31]. It should be noticed that the 'x' here does not have to be integer to represent the nonstoichiometric oxides [7], whose presence is testified by the increased FWHMs observed here than that from the standard stoichiometric oxides. Based on these observations, it is reasonable to predict that the activation of the getter film has occurred at 150 °C, albeit to a very slight extent. It should be kept in mind that the getter film is only annealed for 1 h, and there is no doubt

that the reduction (activation) will continue with prolonged annealing time considering the temperature only determines the thermodynamics of the activation.

The evolution of Zr 3*d* spectrum with annealing temperature is presented in Fig. 2(b). It is clear that the changes in zirconium spectra with respect to the as-deposited sample during annealing at 150 ˚C also involves shifting towards lower binding energy, indicating the commencement on the reduction of the initially formed native oxides on the superficial surface of the getter film, but such reduction process has not been completed as no peaks are observed around BE = 179 eV (representing the metallic Zr^0). The incomplete reduction process is also testified by the broadening of the Zr 3*d* peaks. When annealed at 160 ˚C, apart from the shift of the peaks towards the lower binding energy, a new shoulder appears at lower binding energy around 178.7 eV, suggesting the formation of species with zirconium of lower valence states. Further increasing the temperature to 170 ˚C does not induce too much changes to the resulting XPS spectrum while the portion of the freshly formed shoulder increases when the annealing temperature is increased to 180 ˚C.

As shown in Fig. 2(c), the V 2*p* spectrum experiences the most rapid evolution compared with its Ti 2p and Zr 3d counterparts. Upon annealing at as low as 150 ˚C, the peak at binding energy of 517.1 eV disappears with the presence of a fresh peak at much lower binding energy. Increasing the annealing temperature to 170 ˚C, the fresh peak grows gradually and remains almost unchanged beyond 170 ˚C.

The XPS spectrum collected from the C 1*s* core level orbital also varies with the annealing temperature, as shown in Fig. 2(d). After one hour's baking at 150 ˚C, the main peak at BE = 284.3 eV associated with adventitious carbon in the as-deposited getter film has shifted a little bit by 0.2 eV to 284.5 eV, and the shoulder initially observed at BE = 287.3 eV totally vanished. The characteristics of the spectrum remain almost unchanged even when the annealing temperature is further increased to 160 ˚C. Annealing at 170 ˚C produces a new peak at BE = 281.3 eV apart from the existing peak at BE = 284.3 eV. After being annealed at 180 ˚C, the 281.3 eV peak becomes stronger as compared with the 284.3 eV peak.

To quantitatively evaluating the abovementioned changes induced by annealing at different temperatures, the corresponding spectra have been modelled with the prescribed peak constrains, and the modelling results are exhibited in Fig. 3. Only the modelling results of the spectra collected from the as-deposited samples and that annealed at 150 ˚C and 180 ˚C are included in Fig. 3 as to reveal the corresponding chemical states on the superficial surface of the initial state, directly upon commencement and completion of activation, respectively.

Deconvolution of the Ti 2*p* spectrum collected from the 150 ˚C annealed sample reveals that apart from the TiO_2 (Ti(IV))and Ti_2O_3 (Ti (III)) species, appreciable amount of TiO (Ti(II)) compounds are formed at 150 ˚C, as characterized by the deconvoluted 2*p*3/2 peak at BE = 453.7 eV with FWHM of 2.3 eV (Fig. 3). Other than the dominance of Ti(IV) over Ti(III) in the as-deposited sample, their relatively amount has been reversed in the 150 ˚C annealed sample. The fractions of Ti(IV), Ti(III) and Ti(II) accounts for 22.5%, 64.5% and 13.0%, respectively. When the annealing temperature increases to 160 ˚C, an additional 2*p*3/2 peak at a binding energy of 453.4 eV (FWHM = 1.67 eV) can be resolved, suggesting the reduction of titanium oxides to its metallic state (Ti^0, 14.1%). In parallel, the fraction of Ti(IV) and Ti(III) is reduced to 8.9%, 35.5% respectively, while the Ti (II) fraction drastically increased to 41.5%. After resolving the Ti 2*p* spectrum collected at 170 ˚C, no 2*p*3/2 peaks associated with Ti(IV) and Ti(III) can be resolved. The comparison on the peaks areas of Ti^0 and Ti (II) shows that majority of the titanium oxides have been reduced to Ti^0 (83.3%) with Ti(II) accounts for a fraction 16.7%. Such valence states and their fractions of Ti atoms does not change too much when the getter films is finally annealed at 180 ˚C after resolving the collected 2*p* spectrum, as shown in the first column of Fig. 3.

Quantitative comparison of the Zr3*d* spectrum at various annealing temperatures is exhibited in the second column of Fig. 3. When the getter films is annealed at 150 ˚C, the most significant changes regarding the Zr3*d* peaks involves the appearance of Zr_2O_3 (Zr(III)) with a characteristic 3*d*5/2 peak resolved at BE = 181.5 eV (FWHM = 1.8 eV). The $Zr(OH)_4$ component observed in the as-deposited getter film totally disappears at this temperature, while the components of ZrO (Zr(II)) and ZrO_2 (Zr(IV)) remain with their respective fraction reversed. The fractions accounted by Zr (IV) and Zr(II) are 20.4% and 4.3%, respectively. The rest fraction (75.3%) exists in the form of Zr(III). When the getter film is further annealed at 160 ˚C, the oxides are further reduced causing the disappearance of Zr(IV) and Zr(III) components. At this temperature, metallic/carbidic, Zr^0/ZrC, starts to appear with the 3*d*5/2 peak at BE of 178.5 eV with FWHM = 1.84 eV. The areas underlying the resolved peaks indicates that about 28% of Zr atoms have been reduced to its metallic state Zr^0, and the rest (72.0%) still remains in its lower valence state (Zr(II)). Increasing the annealing temperature up to 180 ˚C, the main components resolved from the spectrum remain unchanged, Zr(II) and Zr^0, the share of Zr^0 gradually increases to 36.0% and 41.0%, respectively at 170 ˚C and 180 ˚C.

The V2*p* spectrum has also been resolved to disclose the valence states evolution with annealing temperature, the results are displayed in the third column of Fig. 3. At 150 ˚C, the initial V_2O_5 and VO_2 oxides are completely reduced, leading to a coexistence of various vanadium oxides (VO (V(II)) and V_2O_3 (V(III))) with metallic vanadium (V^0). The three species, V(II), V(III) and V^0, are testified by the characteristic 2*p* peaks at binding energy of 513.99 eV (FWHM = 2.16 eV), 515.35 eV (FWHM = 4.0 eV) and 512.04 eV (FWHM = 1.30 eV), respectively. Coexistence of these three species persist as the annealing temperature increases to 160 ˚C. However, when the temperature is increased to ≧170 ˚C, the oxide species (V(II) and V(III)) totally vanished and all of the V atoms within the superficial surface are completely reduced to V^0.

Upon annealing at 150 ˚C, the decomposition of carboxyl species attached on the initial surface takes place, as its characteristic XPS peak vanishes (Fig. 3). The C 1*s* peak arising from the adventitious C remains and persists even when the temperature is increased to 180 ˚C. However, at 170 ˚C, an additional peak at BE = 281.31 eV (FWHM = 2.03 eV) is resolved, indicating the formation of metallic carbides at this temperature, as in consistent with the formation of ZrC. An increase in the intensity of such carbide C 1*s* peak is also derived when the temperature is increased to 180 ˚C.

Based on the abovementioned analysis, the fraction evolution of various valence states of each metallic element with annealing temperature has been summarized, as shown in Fig. 4. The fraction of Zr atoms combined in $Zr(OH)_4$ is added to that of ZrO_2 to reveal the total share of Zr with a valence of 4. The share of the high valence states (Ti (IV), Zr(IV) and V(V) + V(IV)) of the three elements all present similar decreasing trend and finally become zero as the temperature increases. But the critical temperature at which this zero fraction is achieved is different, and follows the decreasing order as Ti(IV) (170 ˚C) > Zr (IV) (160 ˚C) > V(V) + V(IV) (150 ˚C). The characteristics of the curves representing the fraction evolution of the medium valence states, M(n) (M = Ti/Zr/V, 1 < n < 4) are quite similar. The respective curves all possess a turning point, before which their shares increase with annealing temperature, and decreases afterwards. Such turning point comes at higher temperature for M(II) other than M(III). As the annealing temperature increases, the share of M^0 is monotonically increased immediately after its formation temperature is reached. Such temperature, however, is different among the studied elements (Ti, Zr and V). Specifically, Ti^0 and Zr^0 first appears at a temperature 150 ˚C < T < 160 ˚C, while that for V^0 is obviously lower at < 150 ˚C (It is not practical to derive the exact temperature in the present study because the corresponding XPS spectra at temperatures < 150 ˚C is not collected). Based on the sequence of their appearance, it is clear that the metallic oxides (TiO_2, ZrO_2 and V_2O_5 + VO_2) are reduced in steps, like, $TiO_2 \rightarrow Ti_2O_3 \rightarrow TiO \rightarrow Ti$, subjected to annealing

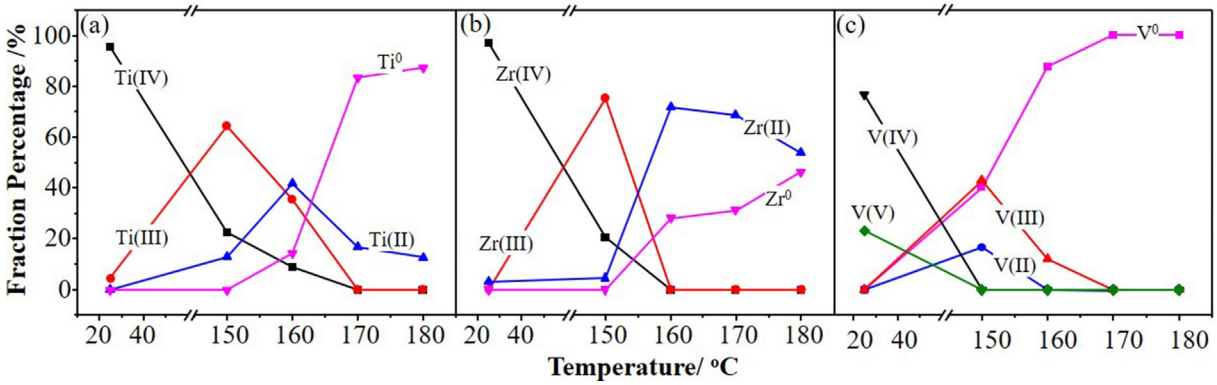

Fig. 4. Valence states evolution of (a) Ti, (b) Zr and (c) V with increasing annealing temperatures.

treatment. Such reduction behavior has also been reported in [32]. In addition, it is straightforward that the vanadium oxides (V(V) and V (IV)) are the first to be reduced with increasing annealing temperature, which is consistent with the existing literature [16,33,34]. A simple comparison of the shares of Ti^0 and Zr^0 (87% vs. 46%) at 180 °C may conclude that the zirconium dioxide is the least easiest to be reduced, such observation is also in agreement with that reported by et. al. [32] who claimed higher reduction resistance from ZrO_2 subjected to annealing. In this regards, the observed stabilities of the metallic oxides follow this order: ZrO_2 > TiO_2 > V_2O_5, such observations are consistent with that presented by Ellingham Diagrams [35]. Considering the occurrence of significant changes regarding the fraction of various valence states of Ti, Zr and V, it is safe to claim that activation process of the studied thin film commences at 150 °C.

4. Conclusions

A Ti-Zr-V getter film was deposited on OFC substrate, and its microstructural characteristics are investigated. The activation process was studied by In-situ synchrotron radiation X-ray photoelectron spectroscopy while being annealed at different temperatures, the evolution of chemical states with increasing annealing temperature on the superficial surface of the film were quantitatively evaluated by resolving the collected XPS spectra. The main findings are as follows:

(1) Microstructural characterization discloses a porous and rough (Ra 59.2 nm) surface from the getter film with a porosity of around 5%. The film is composed of 29.5 at.% Ti, 29.8 at.% V, 33.2 at.% Zr and 7.5 at.% O. The three metallic elements are homogenously distributed within the film bulk.
(2) The as-deposited film are covered by stable metallic oxides, TiO_2, ZrO_2 and V_2O_5 + VO_2, which are reduced in steps upon annealing treatment through their suboxides of intermediate valence states to final metallic states. The ease of the reduction follows the descending order, V_2O_5 > TiO_2 > ZrO_2.
(3) The activation of the thin film starts at a temperature as low as 150 °C, at which about 40% of vanadium atoms contained in the surface of the film have been reduced to its metallic state.

Declaration of Competing Interest

The authors declare that they have no known competing financial interests or personal relationships that could have appeared to influence the work reported in this paper.

Acknowledgements

This work was supported by the National Natural Science Foundation of China (11905219), the Fundamental Research Funds for the Central Universities (WK2310000071) and the National Key Research and Development Program of China (2016YFA0402004).

References

[1] L. Tenchine, X. Baillin, C. Faure, P. Nicolas, E. Martinez, A.-M. Papon, NEG thin films for under controlled atmosphere MEMS packaging, Sens. Actuators A 172 (1) (2011) 233–239.
[2] K. Chuntonov, J. Setina, G. Douglass, The newest getter technologies: materials, processes, equipment, J. Mater. Sci. Chem. Eng. 3 (09) (2015) 57.
[3] C. Benvenuti, P. Chiggiato, F. Cicoira, Y. L'Aminot, Nonevaporable getter films for ultrahigh vacuum applications, J. Vac. Sci. Technol. A 16 (1) (1998) 148–154.
[4] C. Benvenuti, P. Chiggiato, P.C. Pinto, A.E. Santana, T. Hedley, A. Mongelluzzo, V. Ruzinov, I. Wevers, Vacuum properties of TiZrV non-evaporable getter films, Vacuum 60 (1–2) (2001) 57–65.
[5] K. Mašek, F.e. Šutara, T. Skála, J. Drbohlav, K.i. Veltruská, V.r. Matolín, X-ray photoelectron spectroscopy and static secondary ion mass spectroscopy study of activation mechanism of Zr–V low activation temperature nonevaporable getter films, J. Vac. Sci. Technol. A 21 (3) (2003) 797–805.
[6] M. Sancrotti, G. Trezzi, P. Manini, An x-ray photoemission spectroscopy investigation of thermal activation induced changes in surface composition and chemical bonds of two gettering alloys: Zr2Fe versus Zr57V36Fe7, J. Vac. Sci. Technol., A 9 (2) (1991) 182–189.
[7] Z. Abboud, O. Moutanabbir, Temperature-dependent in situ studies of volatile molecule trapping in low-temperature-activated Zr alloy-based getters, J. Phys. Chem. C 121 (6) (2017) 3381–3396.
[8] O. Malyshev, K. Middleman, J. Colligon, R. Valizadeh, Activation and measurement of nonevaporable getter films, J. Vac. Sci. Technol. A 27 (2) (2009) 321–327.
[9] O.B. Malyshev, R. Valizadeh, J.S. Colligon, A. Hannah, K.J. Middleman, S. Patel, V.M. Vishnyakov, Influence of deposition pressure and pulsed dc sputtering on pumping properties of Ti–Zr–V nonevaporable getter films, J. Vac. Sci. Technol. A 27 (3) (2009) 521–530.
[10] O.B. Malyshev, Vacuum in Particle Accelerators: Modelling, Design and Operation of Beam Vacuum Systems, John Wiley & Sons, 2020.
[11] A. Prodromides, C. Scheuerlein, M. Taborelli, Lowering the activation temperature of TiZrV non-evaporable getter films, Vacuum 60 (1–2) (2001) 35–41.
[12] C. Benvenuti, J.M. Cazeneuve, P. Chiggiato, F. Cicoira, A. Escudeiro Santana, V. Johanek, V. Ruzinov, J. Fraxedas, A novel route to extreme vacua: the non-evaporable getter thin film coatings, Vacuum 53 (1) (1999) 219–225.
[13] W.D. Jenkins, T.G. Digges, C.R. Johnson, Tensile properties of copper, nickel, and 70-percent-copper-30-percent-nickel and 30-percent-copper-70-percent-nickel alloys at high temperatures, J. Res. Nat. Bur. Stand. 58 (4) (1957) 201–211.
[14] C. Benvenuti, P. Chiggiato, F. Cicoira, V. Ruzinov, Decreasing surface outgassing by thin film getter coatings, Vacuum 50 (1) (1998) 57–63.
[15] C. Benvenuti, P. Chiggiato, A. Mongelluzzo, A. Prodromides, V. Ruzinov, C. Scheuerlein, M. Taborelli, F. Lévy, Influence of the elemental composition and crystal structure on the vacuum properties of Ti–Zr–V nonevaporable getter films, J. Vac. Sci. Technol. A 19 (6) (2001) 2925–2930.
[16] C.-C. Li, J.-L. Huang, R.-J. Lin, C.-H. Chen, D.-F. Lii, Characterization of activated non-evaporable porous Ti and Ti–Zr–V getter films by synchrotron radiation photoemission spectroscopy, Thin Solid Films 515 (3) (2006) 1121–1125.
[17] C. Benvenuti, P. Chiggiato, P. Costa Pinto, A. Escudeiro Santana, T. Hedley, A. Mongelluzzo, V. Ruzinov, I. Wevers, Vacuum properties of TiZrV non-evaporable getter films, Vacuum 60 (1) (2001) 57–65.
[18] A.E. Prodromides, C. Scheuerlein, M. Taborelli, The characterisation of non-evaporable getters by Auger electron spectroscopy: analytical potential and artefacts, Appl. Surf. Sci. 191 (1) (2002) 300–312.
[19] Z. Abboud, In situ studies of volatile molecules trapping in zirconium alloy-based non-evaporable getter, École Polytechnique de Montréal (2016).
[20] R. Sharma, S. Bhattacharya, R. Tokas, K. Bhushan, S. Sen, S. Gadkari, S. Gupta, Deposition and in-situ characterization of Ti–Zr–V alloy thin films annealed at different temperatures under ultra-high vacuum conditions, J. Alloys Compd. 651 (2015) 375–381.

[21] O. Almén, G. Bruce, Sputtering experiments in the high energy region, Nucl. Instrum. Methods 11 (1961) 279–289.
[22] M.C. Biesinger, L.W. Lau, A.R. Gerson, R.S.C. Smart, Resolving surface chemical states in XPS analysis of first row transition metals, oxides and hydroxides: Sc, Ti, V, Cu and Zn, Appl. Surf. Sci. 257 (3) (2010) 887–898.
[23] D. Briggs, Handbook of X-ray Photoelectron Spectroscopy CD Wanger, WM Riggs, LE Davis, JF Moulder and GE Muilenberg Perkin-Elmer Corp., Physical Electronics Division, Eden Prairie, Minnesota, USA, 1979. 190 pp. $195, Surface and Interface Analysis 3(4) (1981) v-v.
[24] J.A. Thornton, High rate thick film growth, Annu. Rev. Mater. Sci. 7 (1) (1977) 239–260.
[25] P.S. Bagus, C.J. Nelin, C.R. Brundle, S.A. Chambers, A new mechanism for XPS line broadening: the 2p-XPS of Ti(IV), J. Phys. Chem. C 123 (13) (2019) 7705–7716.
[26] C. Sittig, M. Textor, N.D. Spencer, M. Wieland, P.H. Vallotton, Surface characterization of implant materials c.p. Ti, Ti-6Al-7Nb and Ti-6Al-4V with different pretreatments, J. Mater. Sci. Mater. Med. 10 (1) (1999) 35–46.
[27] G. Lu, S.L. Bernasek, J. Schwartz, Oxidation of a polycrystalline titanium surface by oxygen and water, Surf. Sci. 458 (1) (2000) 80–90.
[28] D. Petti, M. Cantoni, M. Leone, R. Bertacco, E. Rizzi, Activation of Zr–Co–rare earth getter films: An XPS study, Appl. Surf. Sci. 256 (21) (2010) 6291–6296.
[29] I. Fongkaew, R. Akrobetu, A. Sehirlioglu, A. Voevodin, S. Limpijumnong, W.R.L. Lambrecht, Core-level binding energy shifts as a tool to study surface processes on LaAlO3/SrTiO3, J. Electron. Spectrosc. Relat. Phenom. 218 (2017) 21–29.
[30] L.-H. Wu, T.-C. Lin, C.-M. Cheng, C.-C. Chang, C.-K. Chan, S.-Y. Perng, I.C. Sheng, Comparative study of Ar-implanted Ti-Zr-V non-evaporable getter films on the Al-alloy substrate, AIP Adv. 8 (7) (2018) 075025.
[31] C.J. Nelin, P.S. Bagus, M.A. Brown, M. Sterrer, H.J. Freund, Analysis of the broadening of X-ray photoelectron spectroscopy peaks for ionic crystals, Angew. Chem. Int. Ed. 50 (43) (2011) 10174–10177.
[32] J. Zemek, P. Jiricek, XPS and He II photoelectron yield study of the activation process in Ti–Zr NEG films, Vacuum 71 (1) (2003) 329–333.
[33] J. Kovac, O. Sakho, P. Manini, M. Sancrotti, Near-surface chemistry in Zr 2 Fe and ZrVFe studied by means of X-ray photoemission spectroscopy: a temperature-dependent study, J. Vac. Sci. Technol. A 18 (6) (2000) 2950–2956.
[34] V. Matolín, V. Dudr, S. Fabík, V. Cháb, K. Mašek, I. Matolínová, K.C. Prince, T. Skála, F. Šutara, N. Tsud, K. Veltruská, Activation of binary Zr–V non-evaporable getters: synchrotron radiation photoemission study, Appl. Surf. Sci. 243 (1) (2005) 106–112.
[35] J.H.E. Jeffes, Ellingham Diagrams, in: K.H.J. Buschow, R.W. Cahn, M.C. Flemings, B. Ilschner, E.J. Kramer, S. Mahajan, P. Veyssière (Eds.), Encyclopedia of Materials: Science and Technology, Elsevier, Oxford, 2001, pp. 2751–2753.